Dynamic Article Links >

FEATURE ARTICLE

Engineering nanostructured electrodes away from equilibrium for lithium-ion batteries

Yanyi Liu, Dawei Liu, Qifeng Zhang and Guozhong Cao*

Boosted by the rapid advances of science and technology in the field of energy materials, Li-ion batteries have achieved significant progress in energy storage performance since their commercial debut in 1991. The development of nanostructured electrode material is regarded as one of the key potentials for the further advancement in Li-ion batteries. This feature article summarizes our recent efforts in the synthesis and characterization of nanostructured electrode materials for high-performance Li-ion batteries. The electrode materials include manganese oxide nanowall arrays, vanadium oxide nanofibers and films, vanadium oxide–carbon nanocomposites, lithium iron phosphate–carbon nanocomposite films, and titanium oxide nanotube arrays. Enhanced Li^+ intercalation capacities, improved rate capabilities and better cyclic stability were achieved by constructing micro- or nanostructure, controlling materials crystallinity and introducing desired defects on the surface and/or in the bulk. The fabrication of binderless and additive-free nanostructured electrodes for Li-ion batteries *via* sol–gel processing is also highlighted.

1. Introduction

In the 21st century, environmental issues, limited irreversible fossil-fuel supplies and the worldwide thirst for energy have significantly advanced the exploration and development of renewable energy technologies, such as solar cells, wind and hydro-power.[1] However, better energy storage technologies are always key issues due to the requirements of continuity and portability of the power supplies in our modern life with constant motion and desire for uninterrupted connection. Among the

various available technologies for energy storage, Li-ion batteries have become the prime candidates to power the next generation of automobiles, and been listed as serious competitors for small scale decentralized applications such as photovoltaics.[2] This is due to the fact that Li-ion batteries offer the best combination of high energy density, power density and output voltage, and the technology relies on a rich and versatile chemistry providing a wide range of electrode materials resources.[3]

Li-ion batteries are comprised of three primary components: a cathode and an anode separated by an electrolyte, the same device structure as conventional batteries. The most commercially popular electrode materials are graphite or titanium oxide (TiO_2) for the anode, and lithium salts (lithium cobalt oxide,

Department of Materials Science and Engineering, University of Washington, Seattle, WA, 98195, USA

Yanyi Liu is a Ph.D. student under the supervision of Professor Guozhong Cao in the Department of Materials Science and Engineering at University of Washington. Her current research is mainly focused on sol–gel processing and electrochemical characterizations of nanostructured materials for energy storage devices.

Yanyi Liu

Dr Dawei Liu is a postdoc associate under the supervision of Professor Guozhong Cao in Department of Materials Science and Engineering at University of Washington, Seattle, WA. He has published six first-authored refereed papers and one book chapter. His specific research project is focused on nanostructured electrodes for efficient lithium ion intercalation.

Dawei Liu

LiCoO$_2$, lithium manganese oxide, LiMn$_2$O$_4$, or lithium iron phosphates, LiFePO$_4$) or oxides (vanadium pentoxide, V$_2$O$_5$, or manganese dioxide, MnO$_2$) for the cathode. As illustrated schematically in Fig. 1, during discharging of a battery, Li ions are extracted from the anode and diffuse towards the cathode through the non-aqueous electrolyte and a porous separator, and subsequently are intercalated into the cathode, while the electrons are transported from the anode to the cathode via an external circuit. During charging, the Li ions and current flow in the reverse direction, and this is realized by applying a certain voltage from an external electrical power supply.[4] The reactions within a Li-ion battery composed of LiFePO$_4$ as cathode and TiO$_2$ as anode can be written as eqn (1)–(3):

$$Cathode: \text{LiFePO}_4 \leftrightarrow \text{Li}_{1-x}\text{FePO}_4 + x\,\text{Li}^+ + x\,e^- \quad (1)$$

$$Anode: \text{TiO}_2 + x\,\text{Li}^+ + x\,e^- \leftrightarrow \text{Li}_x\text{TiO}_2 \quad (2)$$

$$Overall: \text{LiFePO}_4 + \text{TiO}_2 \leftrightarrow \text{Li}_{1-x}\text{FePO}_4 + \text{Li}_x\text{TiO}_2 \quad (3)$$
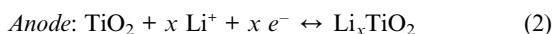
Li-ion batteries store electrical energy as potentially available chemical energy, and the energy storage process in Li-ion batteries requires Faradic oxidation and reduction of the electrochemically active materials to release charges, which can perform electrical work when they flow between two electrodes. The Faradic reactions in Li-ion batteries usually occur with phase changes.[5] Thermodynamically the potential difference between two electrodes of a battery is constant throughout the discharge or charge process (Fig. 2 (a)). In comparison, the charge storage process is non-Faradic in a double-layer capacitor, and the voltage on the capacitor changes linearly with the number of charges. The discharging/charging behavior of ideal batteries and capacitors is shown in Fig. 2 (b). The real discharging/charging curves of electrode materials often show sloping manner, which is related to the crystallinity, crystallite size, crystal structure or intercalation mechanisms. The storage energy of a battery is presented by the area under the potential–capacity curve, and calculated by the integral of the product of potential V and charge Q.

$$E = \int V\,\mathrm{d}Q \quad (4)$$
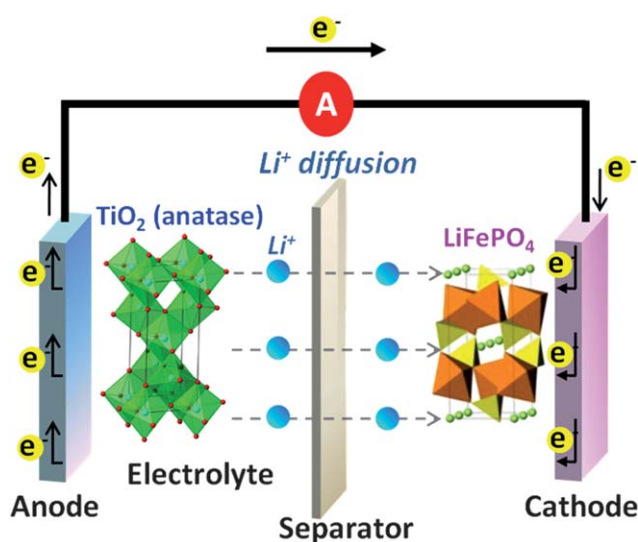
Fig. 1 A schematic drawing showing a complete Li-ion battery. During the discharging process, Li$^+$ diffuse from the anode (negative side) to the cathode (positive side) through the Li$^+$ conducting electrolyte, while electrons flow from the anode to the cathode via an outer circuit.
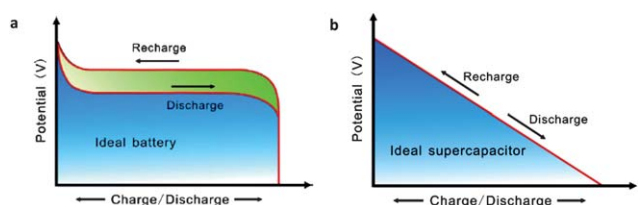
Fig. 2 Comparison of discharge/charge behavior of (a) an ideal battery and (b) an ideal double-layer capacitor.

There are a few criteria which are essential to evaluate and illustrate the characteristics of the materials for Li-ion batteries: Li$^+$ intercalation capacity and energy storage, discharge/charge rate (rate capability) and discharge/charge cycle life (cyclic stability). Li$^+$ intercalation capacity relies on the number of accessible Li$^+$ intercalation sites within the material, and the

Dr Qifeng Zhang is currently working at University of Washington as a Research Assistant Professor. His research interests involve engineering applications of nano-structured materials on electrical devices including solar cells, UV light-emitting diodes (LEDs), field-effect transistors (FETs), and gas sensors.

Qifeng Zhang

Dr Guozhong Cao is Boeing-Steiner Professor of Materials Science and Engineering and Chemical Engineering at the University of Washington. He has published over 250 refereed papers and 5 books including "Nanostructures and Nanomaterials". His current research is focused mainly on nanomaterials for energy conversion and storage.

Guozhong Cao

energy storage is decided by both capacity and working voltage. Rate capability is determined by the kinetics of Li$^+$ diffusion and charge transfer in solid electrodes during Li$^+$ intercalation/deintercalation. The charge and discharge processes in a Li-ion battery often involve irreversible structural or/and phase transformations during interconversion of the electrode materials, which brings about the decay of cycle life in Li-ion batteries. Nanomaterials offer unique mechanical, electrical and optical properties endowed by the confined dimensions with alarge surface area, surface energy and accommodation of volume changes,[6] therefore nanostructured electrode materials for Li-ion batteries have been widely investigated, and high Li$^+$ storage capacities with good rate capabilities and cyclic stabilities were observed.[7–9]

The new concepts of improving electrode materials performance for Li-ion batteries are focused on engineering nanostructures, crystallinity and surface chemistry for enhanced lithium ion intercalation capability.[7,10,11] There have been a good number of studies on nanostructured electrode materials for Li-ion batteries based on the above aspects. The one-dimensional (1D) V$_2$O$_5$ submicro-belts prepared by the sol–gel method exhibited high initial discharge capacity of 346 mAh/g and stayed at 240 mAh/g after 20 cycles.[12] V$_2$O$_5$ nanofibers formed by the electrospinning technique followed by hydrothermal treatment possessed 350 mAh/g electrochemical capacity with close to 100% coulombic efficiency in these V$_2$O$_5$ nanofibers.[13] These nanostructured materials have shown much improved electrochemical properties in comparison with conventional macro- or micro-sized cathode materials for Li-ion batteries.[14,15] LiFePO$_4$ was first synthesized and tested as a cathode material for Li-ion batteries in 1997,[16,17] and it suffered from limited electronic conductivity. Therefore carbon coating[18,19] or aliovalent cation doping[20] have been explored to accelerate the Li$^+$ diffusion and intercalation. For example, the electrochemically deposited carbon coated LiFePO$_4$ (C-LFP)/polypyrrole (PPy) composite cathodes demonstrated 92% of the capacity charged at 0.1 C when rapidly discharged at 10 C (within 6 min).[21] The much enhanced intercalation properties could be attributed to the optimized nanostructure, good electrical conductivity and charge transfer from the carbon defects around LiFePO$_4$ nanoparticles. Various nanostructured MnO$_2$ with different morphologies (nanowires, nanorods, nanoneedles) and phases (α-, β-, γ-) possessed favorable electrochemical properties benefited from the minimized Li$^+$ diffusion distance, poor crystallinity, fast diffusion kinetics and decreased electrode polarization.[22] A novel hierarchically porous MnO$_2$ nanomaterial with a high surface area of 142 m^2 g^{-1} showed very high specific capacitance of 258 F/g and a good reversibility due to its favorable phase, hierarchically porous structure and high surface area.[23]

Conventional Li-ion battery cathode electrode processing includes mixing ~80 wt.% electroactive materials with ~8–10 wt.% conductive additives (typically acetylene black) and ~10–12 wt.% binder (typically poly(vinylidene fluoride), PVDF, dissolved in n-methyl-2-pyrrolidone, NMP, solvent), followed by tape-casting onto current collectors.[24,25] Such fabrication processes are being widely applied in both industrial products and academic studies, however they suffer greatly from the following: (1) increased processing cost and time by complicated multi-processing steps, (2) poor accommodation of mechanical strain and integrity which could decrease the cyclic stability of Li-ion batteries, (3) low volume/mass energy density introduced by electrochemically inactive binders and (4) possible side reactions among binders, additives and active materials during battery cycles affecting intercalation properties.[26] Fabrication of binderless and additive-free film electrodes has been carried out by sputtering,[27] pulsed laser deposition[28] and electrostatic sol-spray deposition.[29] Among all these alternative methods for battery electrode processing methods, the sol–gel based solution method could be one of the most cost-effective ways with easy manipulation and control.

A sol–gel process is a wet-chemical method primarily used for the fabrication of inorganic and organic, crystalline and amorphous materials.[30] A sol refers to a colloidal suspension of very small solid particles in a continuous liquid medium, which could maintain stability under appropriate conditions (concentration, pH value, composition, etc.). A gel is a solid three-dimensional cross-linked network spanning and entangling through the liquid medium due to the surface tension effects, and the network structure may be supported by physical or chemical bonds. Gels can be categorized into different types: hydrogels, organogels, xerogels, etc. A typical sol–gel process consists of two procedures: hydrolysis (eqn (5)) and condensation (eqn (6)), which occur both sequentially and in parallel.[31] Condensation results in the formation of nanoscale clusters, the morphology and microstructure of which could be controlled by manipulating the hydrolysis and condensation reactions.

$$M(OEt)_4 + x\ H_2O \rightarrow M(OEt)_{4-x}(OH)_x + x\ EtOH \quad (5)$$

$$M(OEt)_{4-x}(OH)_x + M(OEt)_{4-x}(OH)_x \rightarrow$$
$$(OEt)_{4-x}(OH)_{x-1}M\text{-}O\text{-}M(OEt)_{4-x}(OH)_{x-1} + H_2O \quad (6)$$
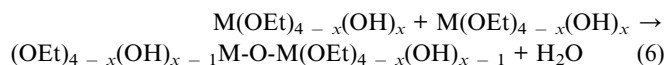
The sol–gel process is a cost effective and low-temperature technique and it realizes fine control and molecular-level homogeneity of the chemical product. The preparation of the precursor sol can be followed by versatile materials fabrication methods in making thin films or other nanostructured materials, for example, dip coating or spin coating thin films on a substrate, synthesis of nanospheres or nanobelts by the hydrothermal method, and acting as the precursors for electrophoretic deposition. The sol–gel process can be diversely used in nanoscience and nanotechnology in the fields of optics, electronics, energy, biosensors and medicine, and it can be applied for the synthesis of complex compounds, which would be difficult for solid-state reaction or other chemical methods.

In a previous feature article, Wang et al.[32] reviewed fabrication of vanadium pentoxide nanorods, nanotubes, core–shell nanocables, and tuning interlayer distance of hydrous vanadium pentoxide thin films for Li-ion batteries via sol–gel processing followed by drop-casting or template-assisted electrodeposition.[33–39] The significantly enhanced Li$^+$ intercalation properties were achieved in the vanadium pentoxide electrodes with special nanostructure designs. In this feature article, we focus on our recent research on various nanostructured electrode materials for Li-ion batteries, including V$_2$O$_5$ nanofibers and nanostructured films, MnO$_2$ nanowall arrays, TiO$_2$ nanotube arrays and LiFePO$_4$–C nanocomposite films. We demonstrate that the much enhanced energy storage properties achieved in

This journal is © The Royal Society of Chemistry 2011

J. Mater. Chem., 2011, **21**, 9969–9983 | 9971

nanostructured electrodes are attributed to (1) large surface energy and surface area for Faradic reactions and easy transport of mass and charges in nanostructured electrodes, (2) poor crystallinity and defects for easy phase transition and larger intercalation capacity, and (3) intimately mixed carbon for better electrical conduction for high specific power. All the electrochemical characterizations were carried out in a standard three-electrode cell, with Pt foil serving as counter electrode, Ag/Ag$^+$ as reference electrode and 1 M LiClO$_4$ in propylene carbonate as the electrolyte. Cyclic voltammetry (CV) and chronopotentiometry (CP) at different current densities and cyclic stability were measured and compared with other reports. More detailed experimental information and electrochemical properties will be discussed in the following sections.

2. Design and fabrication of nanostructured electrodes

It has been widely studied and proved that the nanostructured electrode materials for Li-ion batteries are endowed with these characteristics:[7,11,40,41] (1) short Li$^+$ diffusion path results in faster intercalation/deintercalation process, which brings higher specific power and better electronic/ionic conductivity; (2) high surface area and surface energy provide more electrode–electrolyte contact area, which offers more accessible intercalation sites leading to higher capacity at charge/discharge rate; (3) new thermodynamics and/or kinetics permit enhanced phase transitions and rate capability during Li$^+$ intercalation/deintercalation; (4) better strain accommodation and mechanical integrity during Li$^+$ removal/insertion improve the cyclic stability.

From earlier studies on various nanostructured orthorhombic V$_2$O$_5$: single-crystal V$_2$O$_5$ nanorod arrays,[34–36] V$_2$O$_5$·nH$_2$O nanotube arrays,[37] Ni/V$_2$O$_5$·nH$_2$O core/shell nanocable arrays,[38] V$_2$O$_5$·nH$_2$O films,[33,39] and V$_2$O$_5$/TiO$_2$ composite nanorod arrays and films,[42,43] it was found that by engineering the nanostructure, the intercalation properties and rate performances of vanadium pentoxide electrodes were significantly enhanced in comparison with conventional bulk vanadium oxide electrodes for Li-ion batteries.[32] The improved electrochemical properties could be ascribed to the short Li$^+$ diffusion path, large surface areas as well as the optimized interlayer structure.[44]

Recently we broadened our research interests and efforts into diversified nanostructured electrode materials: mesoporous hydrous MnO$_2$ nanowall arrays,[45,46] mesoporous V$_2$O$_5$ nanofibers,[47] cathodic deposited nanostructured V$_2$O$_5$ films[48] and LiFePO$_4$–carbon nanocomposite films.[49] These nanostructured materials *via* solution-based and template-less fabrication presented enhanced electrochemical properties with high Li$^+$ intercalation capacity and good cyclic stability, which demonstrate their great potential as future electrode materials for Li-ion batteries.

Manganese dioxide (MnO$_2$) can form a wide range of crystalline structures: α-MnO$_2$, ε-MnO$_2$, β-MnO$_2$, γ-MnO$_2$,[50] and due to its high Li$^+$ intercalation capacity of more than 200 mAh/g with good cyclic stability, nanostructured MnO$_2$ has been intensively investigated as promising electrode materials in electrochemical capacitors and Li-ion batteries.[22,23,51–55] In our lab, template-free hydrous MnO$_2$ nanowall array films were deposited at a constant voltage of −1.8 V on a platinum (Pt) coated silicon (Si) wafer on the cathode side out of a 0.1 M concentrated solution with Mn(CH$_2$COO)$_2$·4H$_2$O and Na$_2$SO$_4$ dissolved in deionized (DI) water.[45,46] It was proposed that the growth mechanism of the nanowall arrays was composed of the three following steps: (1) electrolysis of water at the cathode surface (eqn (7)), (2) increase in local pH in the vicinity of the cathode which induced precipitation of Mn(OH)$_2$ on the cathode (eqn (8)) and (3) oxidation of unstable Mn(OH)$_2$ into stable hydrous manganese dioxide MnO$_2$·0.5H$_2$O (eqn (9)) (Fig. 3 (a)).

$$2 \text{ H}_2\text{O} + 2\text{e}^- \rightarrow \text{H}_2 + 2 \text{ OH}^- \tag{7}$$

$$\text{Mn}^{2+} + 2 \text{ OH}^- \rightarrow \text{Mn(OH)}_2 \tag{8}$$

$$2 \text{ Mn(OH)}_2 + \text{O}_2 \rightarrow 2 \text{ MnO}_2 + 2 \text{ H}_2\text{O} \tag{9}$$
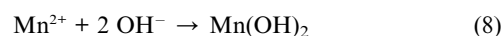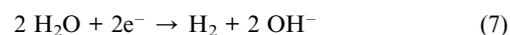
The SEM and TEM images in Fig. 3 (b,c) show the hierarchically grown highly porous nanostructured hydrous MnO$_2$ nanowalls were composed of closely stacked spherical nanoparticles of 50 nm. A large Brunauer–Emmett–Teller (BET) surface area of 96.2 m^2 g^{-1} with a pore size distribution centered at a diameter of 4.2 nm were measured, and this surface area was higher than the template-fabricated mesoporous MnO$_2$ around 91 m^2 g^{-1},[56] MnO$_2$ nanowires of ∼69 m^2 g^{-1}[57] and self-assembled mesoporous-nanostructured manganese oxide of ∼70 m^2 g^{-1}.[58]

It was observed that the cathodic deposited MnO$_2$ nanowall array films prepared at −1.8 V in 0.1 M precursor with a thickness of 500 nm possessed a more favorable hierarchically mesoporous structure with higher discharge capacities and better cyclic stability in comparison with cathodic deposited MnO$_2$ nanowall arrays of other thicknesses or the anodic deposited
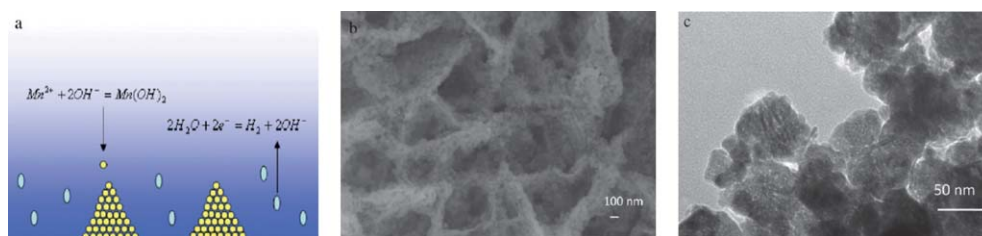
Fig. 3 (a) Schematic drawing of the proposed growth mechanisms of hierarchically porous hydrous MnO$_2$ nanowall arrays derived from cathodic deposition: due to the increased pH value resulting from water electrolysis (blue area has high pH value), the precipitation of Mn(OH)$_2$ nanoparticles from the electrolyte occurred accompanied with the release of H$_2$ gas bubbles at cathode surface; (b) SEM image of hierarchically structured nanowall arrays; (c) TEM image of stacked nanoparticles in a nanowall with voids (pores).[46]
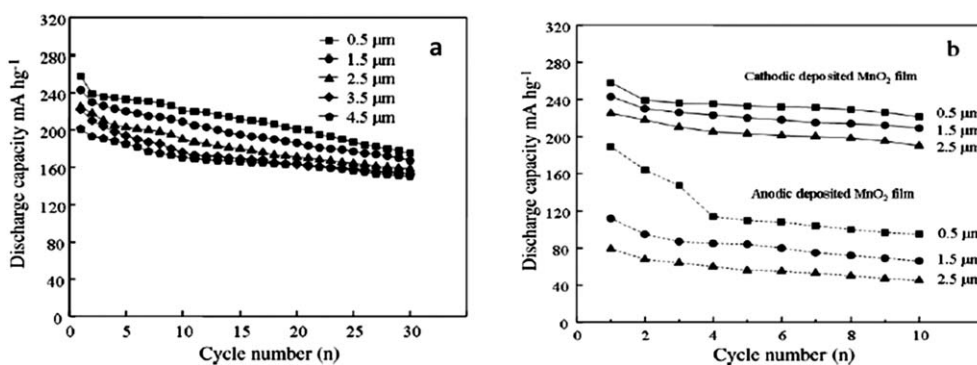
Fig. 4 Comparisons of discharge capacities of cathodic deposited MnO_2 nanowall arrays (a) of different thicknesses for 30 cycles; (b) with anodic deposited MnO_2 in the first 10 cycles.[46]

MnO_2 (Fig. 4(a,b)). The initial capacity was as high as 256 mAh/g, then dropped to 239 mAh/g in the second cycle and remained at 175 mAh/g after 30 cycles.[46] The high discharge capacities were related with the nanowall array structure with large surface area and short diffusion path which are advantageous for intercalation/deintercalation. The cyclic stability improvement could be attributed to the mesoporous nanostructure of cathodic deposited MnO_2 nanowall arrays, which could accommodate more strain and provide mechanical integrity during Li^+ insertion/extraction. Moreover the honeycomb macroporous structure could facilitate the penetration and accessibility of electrolyte to the bottom of the arrays.[59–63]

Vanadium oxide (V_2O_5) is one of the strong and favorable competitors for cathode materials in Li-ion batteries, due to the high Li^+ intercalation capacity (theoretical capacity 450 mAh/g), faster discharge/charge rate, easy fabrication method and good cyclic stability during Li^+ intercalation.[64–72] Electrospinning is a versatile and popular method to fabricate a rich variety of nanostructured ultra-thin fibers, including organic, inorganic and composite materials.[73] In our lab, mesoporous vanadium pentoxide nanofibers were fabricated using a combination of electrospinning and sol–gel methods. The precursor for electrospinning was prepared from V_2O_5 powders, H_2O_2 and poly (vinylpyrrolidone) (PVP) via the sol–gel route. The as-spun V_2O_5 nanofibers were collected on Pt foils and further annealed in air at 500 °C for 1 h, as shown in the SEM images in Fig. 5 (a,b).[47] The yellowish nanofibers were ~350 nm in diameter and tens of microns in length and consisted of interconnected nano-sized platelet particles with highly porous structure. The V_2O_5 nanofibers presented pure orthorhombic phase with interplanar distance and grain size estimated to be ~4.37 Å and 15.5 nm
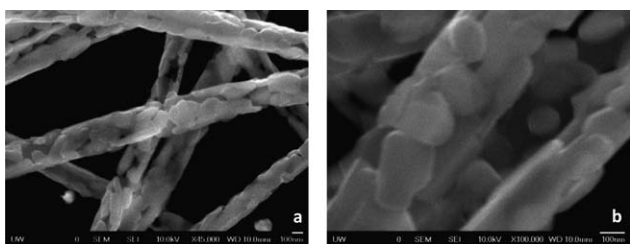
respectively. A large BET surface area of 97 m^2 g^{-1} with the pore size distribution centered at a diameter of 4–5 nm confirmed the mesoporous structure composed of non-rigid aggregates of platelet-like particles or assemblages of slit-shaped pores, which were in good agreement with SEM observations.[74,75]

Fig. 6 (a) presents the CP curves of mesoporous V_2O_5 nanofibers in the 1st cycle tested in a voltage range between −0.5 V and 0.1 V (vs. Ag/AgCl) at a current density of 625 mAh/g. The two well-defined plateaus in the −0.4 V to −0.3 V and −0.2 V to −0.1 V regions revealed the facilitated phase transitions during Li^+ insertion/removal processes in this mesoporous nanostructure. The initial discharge and charge capacities were 377 mAh/g and 372 mAh/g respectively. The charge/discharge capacity of mesoporous V_2O_5 nanofibers remained at 347 mAh/g for the 10th cycle and a loss of 0.78% of the capacity per cycle was observed for the following 30 cycles (Fig. 6(b)), which demonstrated the higher Li^+ intercalation capacity with better cyclic stability in comparison with other nanostructured V_2O_5 cathodes.[33–39] This excellent electrochemical property of V_2O_5 nanofibers cathodes for Li-ion batteries could be attributed to the high surface area and short charge transport distance within 20 nm provided by the mesoporous electro-spun V_2O_5 nanofibers. Moreover the V_2O_5 nanofibers with nanopores could offer a better accommodation for volume change during Li^+ insertion/extraction, and this results in an improved cyclic stability as observed in this study.

As one of the important forms of nanostructured V_2O_5 materials, V_2O_5 films fabricated by various methods have been widely investigated: electrophoretic deposition,[33,35,36] anodic deposition[76] and sputtering,[60] etc. To the best of the authors' knowledge, for the first time, V_2O_5 thin films with unique nanostructures were prepared by means of cathodic deposition from an aqueous solution made from V_2O_5 and H_2O_2. During cathodic deposition, the V^{5+} species from V_2O_5 colloidal particles and dioxovanadate cations, VO_2^+ (generated from V_2O_5 and H_2O_2[77,78]), got reduced on the surface of FTO glass at the negative side (eqn (10–11)), which could serve as nucleation centers initiating and catalyzing the formation of $V_2O_5 \cdot nH_2O$ through low pH conditions (eqn (12)):[76,79,80]

$$V_2O_5 + 4 H^+ \leftrightarrow 2 VO_2^+ + 2 H_2O \qquad (10)$$

$$VO_2^+ + e^- \rightarrow VO_2 \qquad (11)$$

Fig. 5 SEM images of V_2O_5 nanofiber after annealing at 500 °C in air for 1 h (scale bar = 100 nm).[47]

This journal is © The Royal Society of Chemistry 2011

J. Mater. Chem., 2011, **21**, 9969–9983 | 9973
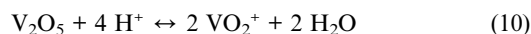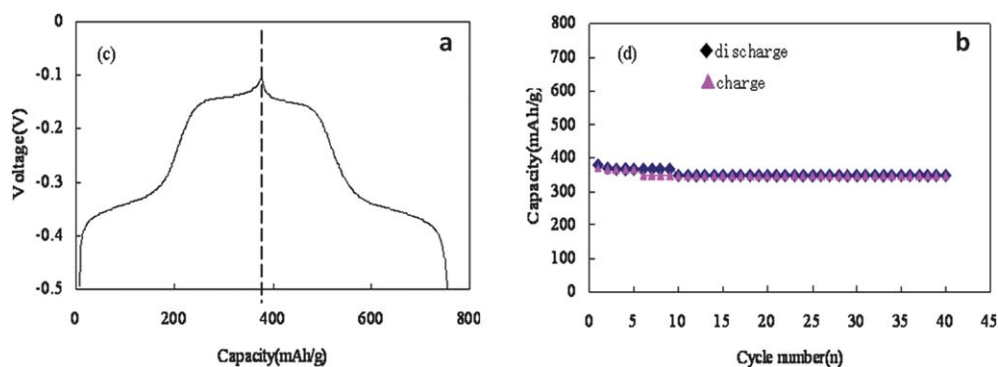
Fig. 6 (a) Chronopotentiometric discharge–charge curves of mesoporous V_2O_5 nanofibers in the 1st cycle with a current density 625 mA g^{-1}. (b) The discharge/charge capacity of mesoporous V_2O_5 nanofibers as a function of cycle number.[47]

$$2 [VO_2]^+ + nH_2O \rightarrow V_2O_5 \cdot nH_2O + 2 H^+ \quad (12)$$
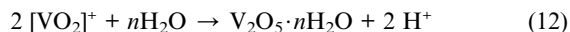
After annealing the as-deposited $V_2O_{5-x} \cdot nH_2O$ films at 500 °C in the air, the V_2O_5 film showed a preferred oriented ortho-rhombic phase with a crystallite size of 35.1 nm calculated from XRD patterns (Fig. 7 (a)).[48] The "wrinkled" nanostructure of V_2O_5 films was detected by SEM to be composed of fine nano-crystallites of 20–30 nm separated by 10 nm gaps as shown in Fig. 7 (b).

The cyclic voltammogram of a 500 °C annealed nano-structured V_2O_5 film in Fig. 8 (a) presented all the cathodic/anodic peaks corresponding to four phase transitions among α, ε, δ, γ, and ω phases within the potential range of 0.6–1.8 V (vs. Ag$^+$/Ag).[65–67] The partially reversible ε/α and δ/ε phase transi-tions were able to be observed in CV and this could become a proof of facilitated thermodynamics and kinetics of phase transitions. The rate capability tests (Fig. 8 (b)) showed high discharge capacities at fast discharge rate: 160 mAh/g at 30 C; 120 mAh/g at 70 C. The high energy density (900 Wh/kg at 1.3 C) and power density (28 kW kg^{-1} at 70 C), enhanced phase tran-sitions as well as the good cyclic stability could be ascribed to the unique nanostructure in this research (Fig. 7 (b)): the 20–30 nm nanocrystallites provided a shorter diffusion path for Li$^+$ inter-calation/deintercalation, and the 10 nm wrinkled gaps offered a higher surface area with more accessible intercalation sites which favored the electrolyte penetration and interface reac-tions.[81,37] This nanostructure could effectively enhance the phase

transition during Li$^+$ intercalation/deintercalation, as shown from CV curves in Fig. 8 (a). This nanostructured V_2O_5 films could also offer more space freedom, therefore the film's mechanical integrity and stability during battery testing could be well maintained which would result in a good cyclic stability.[46]

Lithium iron phosphate (LiFePO$_4$) has been attracting intense interest both in academic and industrial fields because of its high theoretical capacity of 170 mAh/g, flat voltage at ~3.4 V, and good thermal and chemical stability.[16] Moreover it offers economic and environmental advantages of being low cost and less toxic.[82,83] In our lab, uniform and crack-free LiFePO$_4$/C nanocomposite film cathodes were obtained by spreading LiFePO$_4$ sol on a Pt coated Si wafer, followed by ambient drying overnight and annealing/pyrolysis at elevated temperatures in nitrogen gas. The crystallite size was calculated to be 19.4 nm in LiFePO$_4$–C composite films annealed at 600 °C.[49] Fig. 9 (a) shows the SEM image of a 600 °C annealed LiFePO$_4$/C nano-composite film with a homogeneous distribution of carbon particles in the film and some coated on the surface of LiFePO$_4$ particles, which was proved by EDX results.[49] The charge capacity of the LiFePO$_4$/C nanocomposite film for the 1st cycle was 167 mAh/g followed by a discharge capacity of 312 mAh/g (Fig. 9 (b)), showing that the amount of Li$^+$ that intercalated into the film exceeded the theoretical value for stoichiometric crys-talline LiFePO$_4$. The high intercalation performance could be attributed to nanocrystallites sized under 20 nm which could greatly enhance the phase transition during Li$^+$ intercalation/
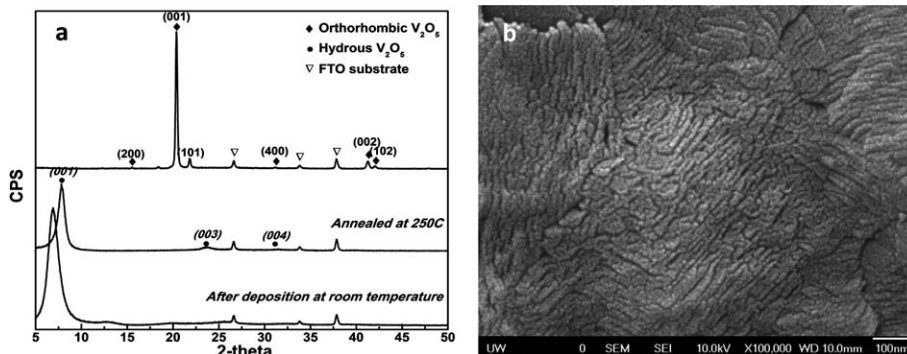
Fig. 7 (a) XRD patterns of the as-deposited $V_2O_{5-x} \cdot nH_2O$ film, hydrous $V_2O_{5-x} \cdot nH_2O$ films annealed at 250 °C and V_2O_5 films annealed at 500 °C in the air. (b) SEM image of the 500 °C annealed V_2O_5 film.[48]
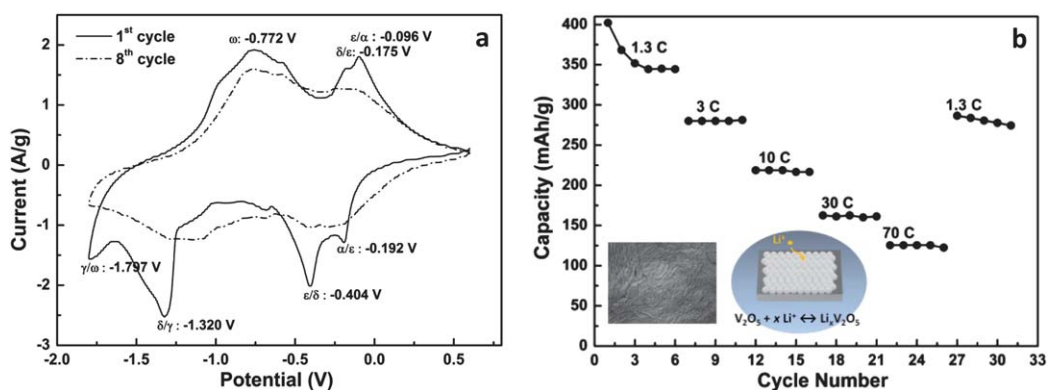
Fig. 8 (a) The cyclic voltammograms of 500 °C annealed V_2O_5 films with a scan rate of 5 mV s^{-1} in 1 M LiClO$_4$/PC electrolyte solution for the 1st cycle (solid line) and 8th cycle (dash-dot line). (b) The discharge capacities of 500 °C annealed V_2O_5 films at various current densities from 200 mA g^{-1} (1.3 C) to 12.5 A g^{-1} (70 C).[48]

deintercalation due to the high surface energy, and favor kinetic processes including a short transport pathway and a high and effective contact area with the electrolyte.[84–86] It has been investigated that for nanomaterials with nano-sized crystallites, the contributions from pseudocapacitance and capacitance to the total storage capacity could become non-negligible.[87–89] For example, the capacitive contribution to the total stored charge in TiO_2 (anatase) nanoparticles could become 55% to 15% when the nanocrystallites were sized 7 nm to 30 nm respectively.[90] The high discharge capacities observed in this study could also be attributed to the pseudocapacitive contribution from $LiFePO_4$ nanocrystallites.

3. Control of crystallinity

As discussed in the first section of this article, well crystallized electrode materials usually assure well defined Faradic redox reactions in electrochemical active materials during Li$^+$ intercalation/deintercalation, as indicated by the long and elegant plateaus in potential–capacity curves (Fig. 2 (a)). However, those electrode materials often suffer from limited capacity or poor rate capability, due to the restricted Li$^+$ diffusion paths and

intercalation sites in the long-range well ordered structure in perfect crystalline materials. Poor crystalline materials with loose packing of ions and lack of long-range ordered structure could offer more open sites for Li$^+$ intercalation which result in high capacity. Poor crystalline materials may also provide better accommodation of volume change during Li$^+$ insertion/extraction, and this could result in more facilitated Li$^+$ intercalation/deintercalation paths with better cyclic stability. There have been some studies on the poor crystalline materials, e.g., ZnSb, MnO_2, with excellent electrochemical performance for the electrodes of Li-ion batteries.[91,92]

Li$^+$ intercalation properties in V_2O_5 have been demonstrated to change appreciably by modifying its crystallinity or interlayer spacing. The addition of 20 mol.% TiO_2 into V_2O_5 films or 25 mol.% TiO_2 into V_2O_5 nanorod arrays retards the crystallization of V_2O_5 as well as the crystallite growth during annealing process, and this results in an almost 100% improvement in Li$^+$ intercalation performance over pure V_2O_5 electrodes.[42,43] It was also found that by controlling the annealing temperatures for $V_2O_5 \cdot n H_2O$ xerogel films, the crystallinity, compositions of crystalline water and interplanar distances could be manipulated to favor the Li$^+$ intercalations.[39] For example, the optimized
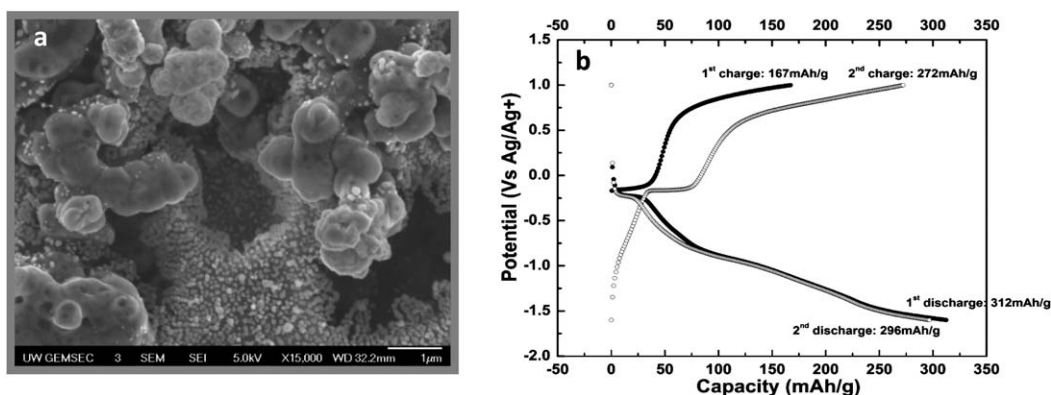
Fig. 9 (a) SEM image of $LiFePO_4$/C nanocomposite films annealed at 600 °C. (b) The first and second charge/discharge curves of sol–gel derived $LiFePO_4$/C nanocomposite cathode films annealed at 600 °C at a discharge rate of 200 mA g^{-1}.[49]

composition $V_2O_5 \cdot 0.3H_2O$ films annealed at 250 °C exhibited the highest initial Li^+ intercalation capacity of 275 mAh/g, and retained a stable capacity of 185 mAh/g after 20 cycles, which was better than the well crystallized orthorhombic V_2O_5 films, or $V_2O_5 \cdot 1.6H_2O$ films at room temperature.

Most recently, we have studied the influence of crystallinity on Li-ion intercalation properties in different electrode materials, for example, LiFePO$_4$/C nanocomposite film cathodes,[49] Mn-doped V_2O_5 films,[93] N_2 annealed V_2O_5 films[94] and TiO$_2$ nanotube arrays,[95] and V_2O_5/carbon nanocomposites.[96] It has been further proved that the kinetics and thermodynamics of materials with controlled crystallinity could be more favored by Li^+ intercalation, which results in higher capacity and better cyclic stability.

Sol–gel processing derived LiFePO$_4$/C nanocomposite film cathodes were annealed in various temperatures from 500 °C to 800 °C in N_2 gas after spreading sols on Pt coated Si wafers.[49] The XRD patterns of LiFePO$_4$/C composite powders annealed at 500 °C, 600 °C, 700 °C and 800 °C are shown in Fig. 10 (a). The powders without annealing were amorphous since there was no detectable peak in the XRD pattern; the patterns of powders annealed at 500 °C, 600 °C, 700 °C and 800 °C exhibited the main peaks of olivine LiFePO$_4$ phase, however with different intensity and shape, which is related to increased crystallinity and ordering of the olivine LiFePO$_4$ phase at elevated annealing temperatures from 500 °C to 800 °C. The growth of crystallite size from 16.1 nm at 500 °C to 30.8 nm at 800 °C could also be calculated from XRD patterns using Scherrer's equation.

The Li^+ intercalation property for LiFePO$_4$/C nanocomposite films annealed at different temperatures (500–800 °C) at 200 mA g^{-1} were tested and are shown in Fig. 10 (b). The film annealed at 600 °C shows the best capacity and cycle stability, as it delivers the highest discharge capacity of 312 mAh/g for the initial cycle, and stays at 218 mAh/g after 20 cycles. In comparison, the 500 °C annealed films delivered a high discharge capacity similar to the 600 °C films, however it is followed by a drastic drop and then poor cyclic stability since the 3rd cycle. The initial Li^+ intercalation capacity for 700 °C and 800 °C films are 228 mAh/g and 120 mAh/g, which decrease to 148 mAh/g and 99 mAh/g after 20 cycles. This series of comparison shows that the LiFePO$_4$/C

nanocomposite films treated at 600 °C with controlled crystallinity possess the most beneficial structure for Li^+ intercalation. The 600 °C films are less compact and more disordered in comparison with the well crystallized phase, thus it provides a more flexible structure which could accommodate more Li^+ and facilitate the diffusion within this structure. The poor cyclic stability within the 500 °C films could be ascribed to the over-loosely packed microstructure which may experience irreversible change or loose contact with current collector with increased cycles. The 700 °C and 800 °C films have more compact and well crystallized structures, which give limited freedom and restricted space for Li^+ diffusion and intercalation, thus lower discharge capacities are observed. The best electrochemical properties in 600 °C films could also be ascribed to the small crystallite size below 20 nm, which favors the kinetics of phase transition during Li^+ intercalation/deintercalation. A reduced crystallite size decreases the polarization associated with electronic and/or ionic resistance, and thus improves the reversible capacity. The larger particles and crystallites in the films annealed at elevated temperatures present as transport limitation both for Li^+ and electron diffusion, which results in capacity loss.

It has been studied that by doping or adding different elements into the V_2O_5 system, the nucleation and crystallite growth could be hindered, resulting in a lower crystallinity compared to the undoped V_2O_5 fabricated under the same conditions. Recently in our lab, stable and homogeneous Mn-doped V_2O_5 films were prepared via sol–gel processing, in which H_2O_2 and V_2O_5 as were used as sol precursors and Mn^{2+} was directly added during sol preparation.[93] The films were dried at ambient temperature followed by annealing in air at 250 °C for 3 h. The XRD patterns (Fig. 11 (a)) showed that the pristine V_2O_5 films possessed diffraction peaks for both hydrous and orthorhombic V_2O_5 phases; while for Mn-doped V_2O_5 films, there was only a diffraction peak designated to hydrous V_2O_5 and the broadened peak represented a poorer crystallinity in comparison with undoped V_2O_5 films. The interlayer distances were calculated to be ∼11.3 Å for Mn-doped V_2O_5 films, slightly larger than ∼11 Å for un-doped V_2O_5 films, which could be due to the doping of larger Mn^{2+} ions into V_2O_5 lattice. The grain size of Mn-doped
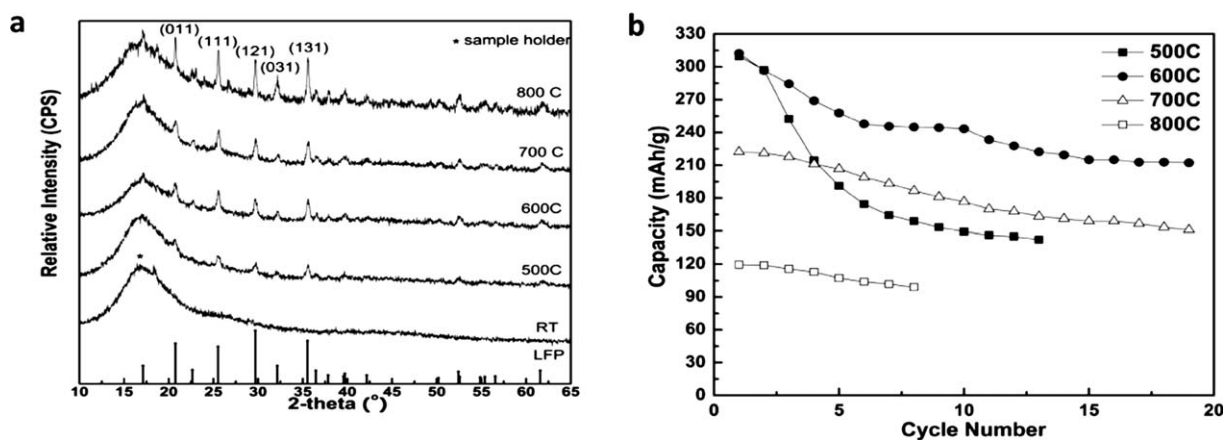
Fig. 10 (a) X-Ray diffraction patterns of sol–gel derived LiFePO$_4$/C composite powders at room temperature and heat treated at 500 °C, 600 °C, 700 °C and 800 °C. (b) Discharge capacities of sol–gel derived LiFePO$_4$/C nanocomposite cathode films annealed at 500–800 °C at a discharge rate of 200 mA g^{-1}.[49]
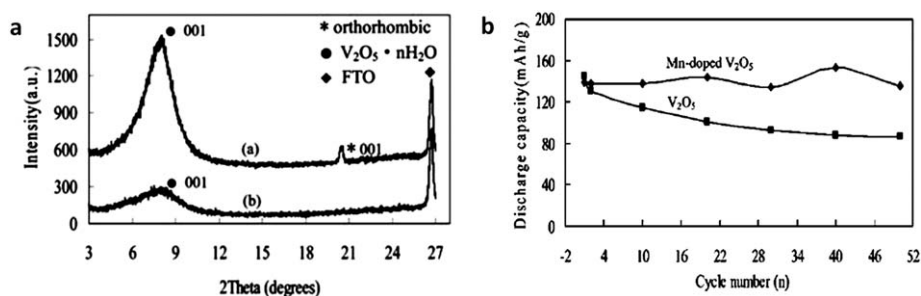
Fig. 11 (a) XRD patterns of a) V_2O_5 films and b) Mn-doped V_2O_5 films. (b) The discharge capacity of V_2O_5 films and Mn-doped V_2O_5 films, at a current density of 680 mA g^{-1}, potential ranging from 0.5 V to −1.4 V vs. Ag/Ag$^+$.[93]

V_2O_5 films was calculated to be ∼1.5 nm from XRD patterns, smaller than the undoped V_2O_5 films with ∼3.5 nm. This showed that the Mn doping has resulted in the suppression of the formation of orthorhombic V_2O_5 and grain growth.[97,98]

The cyclic performance revealed that the Mn-doped V_2O_5 films only lost less than 3.0% of the discharge capacity after 50 cycles, compared with 40% capacity loss for the un-doped V_2O_5 films (Fig. 11 (b)). The improved Li$^+$ intercalation property could be attributed to the effective Mn-doping retarding the nucleation and grain growth during crystallization. The poor crystallinity in the Mn-doped V_2O_5 films could offer more Li$^+$ intercalation sites, and alleviate the strain accompanying the Li$^+$ intercalation/deintercalation. This structure results in a higher Li$^+$ intercalation capacity and better cyclic stability.

Crystallinity could also be manipulated by annealing materials in different gases, which could change the thermodynamic conditions for nucleation and grain growth. V_2O_5 xerogel films were fabricated by spreading V_2O_5 sol onto fluorine doped tin oxide (FTO) glass substrates followed by annealing at 300 °C for 3 h in N_2 and air.[94] In comparison with air annealed V_2O_5 films, N_2 annealed films presented poorer crystallinity judging from the broadened shape and lower intensity of the diffraction peaks (Fig. 12 (a)). The grain size was calculated based on XRD patterns, to be 14.3 nm for air annealed V_2O_5 films, and 5.1 nm for N_2 annealed films. The comparisons of chronopotentiometric curves of air and N_2 annealed V_2O_5 films for the 1st, 20th, and 50th cycle (Fig. 12 (b,c)) show: (1) the lack of plateaus and sloping manner of charge/discharge curves show the evidence of poor crystallinity in N_2 annealed V_2O_5 films; (2) the N_2 annealed

V_2O_5 films start with a low Li$^+$ intercalation capacity (68 mAh/g), which increase to 154 mAh/g at the 20th cycle, and decayed a little to 148 mAh/g at the 50th cycle. This forms a huge contrast with the well crystallized V_2O_5 films, which show a high capacity of 152 mAh/g for the initial cycle, and then dropped drastically to 74 mAh/g and 44 mAh/g at the 20th and 50th cycle. The improved electrochemical property in poor crystalline materials was also found in other materials systems,[99] and it could be ascribed to the poor crystallinity nature and retarded grain size growth after annealing samples in inert gases.

The effect of N_2 annealing and poor crystallinity to electrochemical properties were also confirmed in the study on N_2 annealed TiO_2 nanotube arrays.[95] TiO_2 nanotube arrays were synthesized by anodic oxidation method recorded in reference on titanium foil,[100] followed by calcination from 300 °C to 500 °C for 3 h in N_2 gas. The annealed TiO_2 tube arrays show anatase phase with better crystallinity with increased annealing temperatures. The Li$^+$ discharge capacity and cyclic stability of those TiO_2 tube arrays are compared in Fig. 13. The amorphous as-grown TiO_2 tube arrays show a high initial discharge capacity as 202 mAh/g, however followed by a drastic drop since the 2nd cycle until only 40 mAh/g for the 50th cycle, which shows similar phenomena in amorphous TiO_2 electrodes.[101] The 400 °C and 500 °C annealed TiO_2 tube arrays show much better cyclic stability, however the Li$^+$ discharge capacity is around 160 mAh/g, which is much lower than 300 °C annealed samples. The 300 °C annealed TiO_2 tube arrays possess a high initial discharge capacity of 240 mAh/g, and stay at 148 mAh/g after 50 cycles. The combination of high Li$^+$ storage capacity and good cyclic
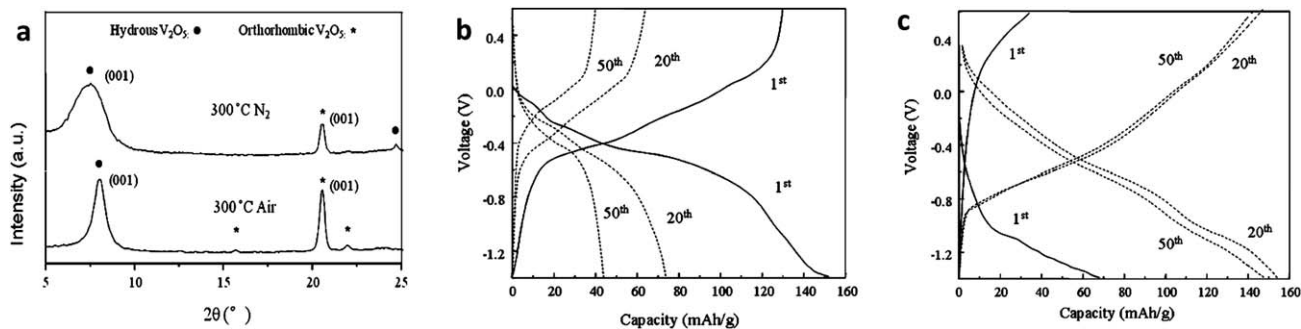
Fig. 12 (a) XRD patterns of V_2O_5 xerogel films annealed in air and nitrogen at 300 °C after 3 h, showing the coexistence of both hydrous and orthorhombic vanadium oxide; Chronopotentiometric discharge/charge curves in the 1st, 20th and 50th cycles at a current density 600 mA g^{-1} of V_2O_5 films annealed in (b) air and (c) nitrogen at 300 °C for 3 h. Potential ranging from 0.6 V to −1.4 V vs. Ag/Ag$^+$.[94]
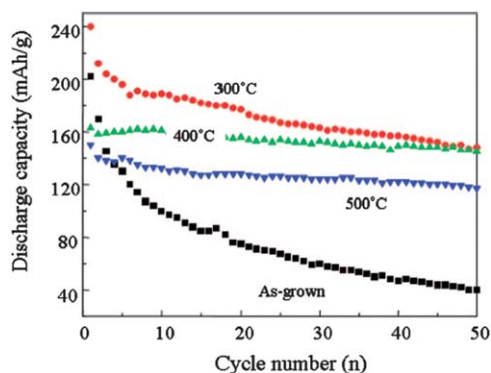
Fig. 13 Li$^+$ intercalation discharge capacity of amorphous as-grown TiO$_2$ nanotube arrays, and anatase TiO$_2$ nanotube arrays annealed at 300, 400, and 500 °C in N$_2$ for 3 h as a function of cyclic numbers. The potential was ranging from −0.6 V to −2.1 V vs. Ag/Ag$^+$ at a current density of 320 mA g^{-1}.[95]

stability could be ascribed to the poor crystallinity in 300 °C annealed TiO$_2$ tube arrays. This poor crystallinity provides better structural support for Li$^+$ insertion/extraction after many cycles in comparison with the loose structure in as-grown amorphous TiO$_2$ nanotubes. It also offers more available Li$^+$ intercalation sites thus results in higher discharge capacity compared with those well crystallized samples.

Coherent hydrous vanadium pentoxide (V$_2$O$_5$·nH$_2$O)–carbon cryogel (CC) nanocomposites were synthesized by dynamic electrodeposition of hydrous vanadium pentoxide onto the porous carbon scaffold, which was derived from resorcinol (R)

and formaldehyde (F) organic hydrogels.[96] The resorcinol–formaldehyde (RF) derived carbon cryogels (CCs) were prepared through a series of processes including gelation, solvent exchange, freeze-drying and pyrolysis,[102–105] then the CCs films were fixed between two Pt meshes and immersed in VOSO$_4$ solution (pH = 1.8) for potentiodynamic electrodeposition, which was carried out at a voltage ranging from 0.6 V to 2.0 V vs. Ag/AgCl for up to 300 cycles.[96] Fig. 14 (a) shows the schematic drawing of synthesis of nanocomposites by electrodeposition of V$_2$O$_5$·nH$_2$O inside the pores of CC films and this reaction (eqn (13)) could be realized in aqueous solution at pH = 1.8 through oxidation of V^{4+} to V^{5+}.[76]

$$2\ VO^{2+} + 3\ H_2O \rightarrow V_2O_5 + 6\ H^+ + 2\ e^- \tag{13}$$
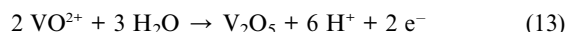
The surface morphologies of as-fabricated V$_2$O$_5$·nH$_2$O–carbon cryogel (CC) nanocomposites were observed to be homogeneous across the sample,[96] which suggested a uniform deposition of V$_2$O$_5$·nH$_2$O throughout the porous carbon cryogel films. This was further proved by pore size distribution derived from nitrogen sorption isotherms (Fig. 14(b)) showing that the peak pore size of CC films of 8 nm decreased to a smaller size of 6 nm after the deposition with a shrunk pore volume from 0.98 cm^3/g to 0.42 cm^3/g. The reduction in the pore volume and pore size were presumably due to the successful deposition of V$_2$O$_5$·nH$_2$O inside the porous carbon cryogel films, which took some of the void space and resulted in the change of the porous structure.
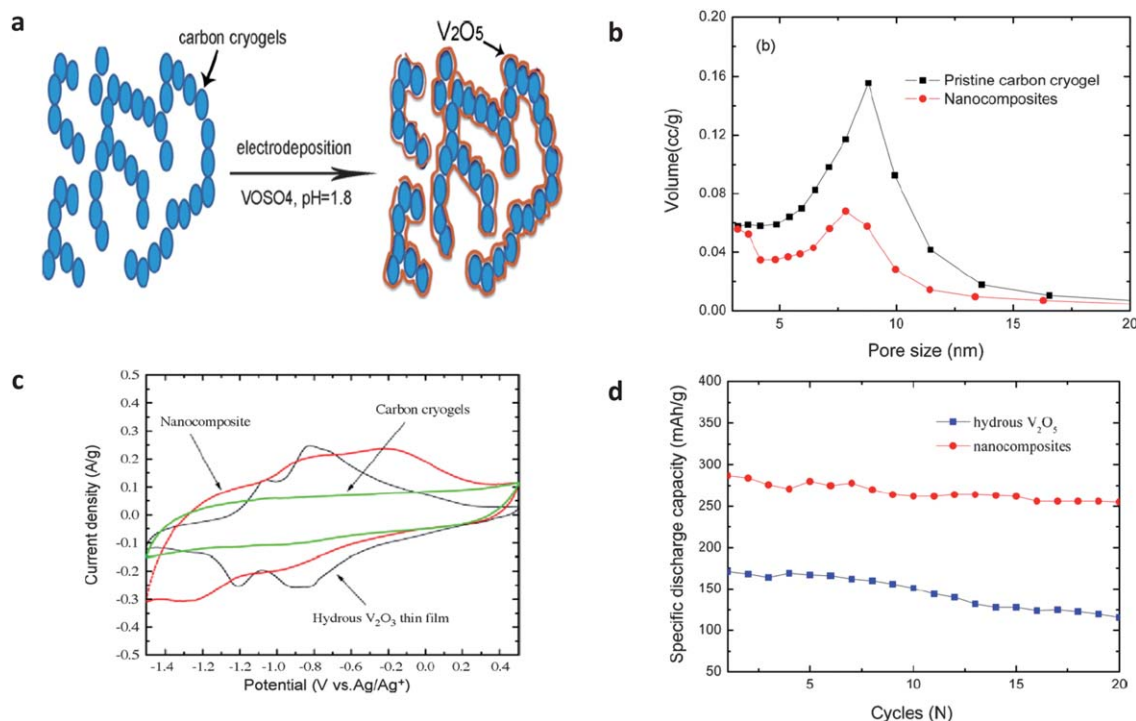
Fig. 14 (a) Schematic drawings of the synthesis and microstructure of coherent nanocomposites in which V$_2$O$_5$·nH$_2$O was deposited and coated onto surface of carbon cryogel scaffold. (b) The pore size distribution of V$_2$O$_5$·nH$_2$O–carbon cryogels by nitrogen sorption isotherms. (c) Cyclic voltammetry curves of hydrous V$_2$O$_5$, carbon cryogel, and V$_2$O$_5$·nH$_2$O–carbon cryogels in the voltage window between 0.5 V and −1.5 V vs. Ag/Ag$^+$ at a scan rate of 1 mV s^{-1}. (d) The specific discharge capacity for V$_2$O$_5$·nH$_2$O–carbon cryogels and V$_2$O$_5$·nH$_2$O as a function of cycle numbers.[96]

Fig. 14 (c) compares the cyclic voltammograms of $V_2O_5 \cdot nH_2O$–CCs nanocomposites, $V_2O_5 \cdot nH_2O$ film and pristine CC film electrodes at voltages ranging from −1.5 V to 0.5 V (*vs.* Ag/Ag$^+$) with a scan rate of 1 mV s^{-1}. Compared with the more distinctive anodic and cathodic peaks related to Li$^+$ intercalation and deintercalation observed in $V_2O_5 \cdot nH_2O$ film, the coherent $V_2O_5 \cdot nH_2O$–CC nanocomposites possessed broader and more overlapped bumps, which could be attributed to the poor crystallinity and different electrochemical potentials of Li$^+$ intercalation/deintercalation caused by dissimilar environments of V_2O_5 surrounded by amorphous CCs. The CC film did not demonstrate any anodic/cathodic peaks related to Li$^+$ intercalation/deintercalation, which could well prove the attribution of $V_2O_5 \cdot nH_2O$ to the Li$^+$ insertion/removal during charge/discharge process. The specific Li$^+$ intercalation capacity of $V_2O_5 \cdot nH_2O$–CC nanocomposites were 280 mAh/g initially and retained 257 mAh/g after 20 cycles, which was higher than the $V_2O_5 \cdot nH_2O$ films showing initial specific capacity of 151 mAh/g and dropped to 96 mAh/g for the 20th cycle as shown in Fig. 14 (d). The much improved electrochemical properties of $V_2O_5 \cdot nH_2O$–CC nanocomposites could be attributed to the shortened mass and charge diffusion distance and enhanced electrical conductivity introduced by the porous carbon cryogel scaffold. This porous nanocomposite structure also improved the reversibility and mechanical support during charge/discharge processes by offering extra accommodation of the stress accompanied with Li$^+$ insertion/removal.[106] The large surface energy and poor crystallinity in $V_2O_5 \cdot nH_2O$–CC nanocomposites could allow easy phase transition and benefit the surface or interface redox reactions, leading to a much expanded range of reversible Li$^+$ intercalation/deintercalation processes.[107,108]\

4. Manipulation of surface chemistry and defects

Electrochemical intercalation comprises of three simultaneous and sequential processes: (1) redox reaction at the interface between electrode and electrolyte; (2) nucleation and growth of new phase starting at the interface; (3) charge and mass transfer from interface to electrode bulk. Surface defects are expected to serve as nucleation sites to promote the phase transitions at the interface between electrode and electrolyte; defects in bulk may favor the propagation or growth of new phases during charge and discharge processes in Li-ion batteries. Therefore, Li$^+$ intercalation capacity and rate capability could be enhanced by manipulating surface chemistry and defects.[109,110] In addition, defects could enhance charge transfer. Annealing samples with reactive gas and substitutional doping are the common routes to manipulate the surface chemistry or introduce defects into the materials.[111] Aside from enhancing Li$^+$ storage energy and improving kinetics, appropriate manipulation of surface chemistry and defects might also protect the nanomaterials on the electrode surface from dissolving into the electrolyte after long-time repeated intercalation/deintercalation cycles, therefore effectively improve the cyclic stability of Li-ion batteries.[10]

We have conducted various experiments recently on the effects of surface chemistry and defects on Li$^+$ intercalation/deintercalation properties: CO gas annealed TiO_2 nanotube arrays,[112] N_2 gas annealed V_2O_5 xerogel films,[94] cathodic deposited V_2O_5 nanostructured thin films,[48] Mn doped V_2O_5 films[93] and LiFePO$_4$/C nanocomposite films.[49] It was found that by manipulating the surface chemistry or introducing defects, the intercalation properties and rate performances could be significantly improved, and this could be ascribed to the facilitated nucleation and phase transitions, as well as enhanced electrical conductivity for charge transfer.

The V_2O_5 xerogel films were annealed at 300 °C for 3 h in N_2 and air.[94] In comparison with air annealed V_2O_5 films, N_2 annealed films presented poorer crystallinity with much smaller grain size. The optical absorption spectra of V_2O_5 films annealed in air and N_2 are shown in Fig. 15 (a) with photographic images in the inset. The dark green color showed in the N_2 annealed V_2O_5 films indicates the presence of V^{4+} and V^{3+} valence states. The comparison of absorption edges suggests a narrower bandgap for N_2 annealed V_2O_5 films, which could be due to the existence of defects in lower valence states. The electrochemical impedance analysis also confirmed an improved electrical conductivity in V_2O_5 films with defects, such as V^{4+}, V^{3+} species and possible associated oxygen vacancies in the N_2 annealed films.

The cyclic stabilities of N_2 and air annealed V_2O_5 films are compared in Fig. 15 (b), and it was found that the discharge
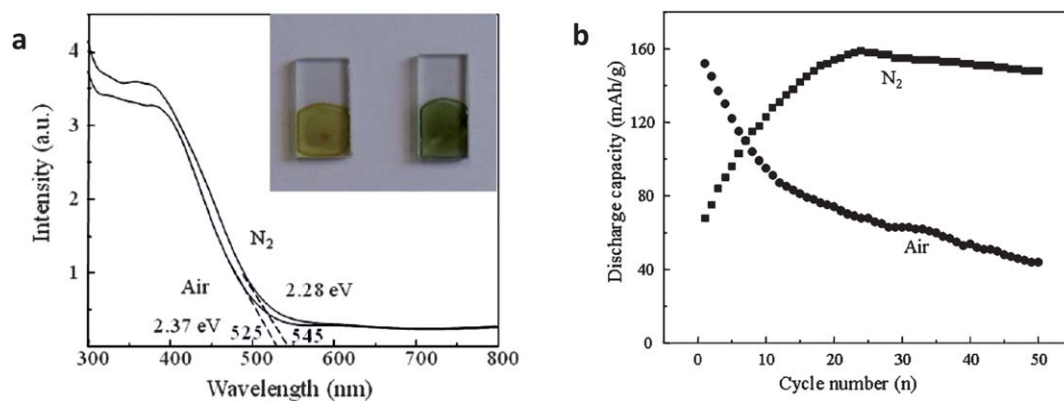
Fig. 15 (a) Absorption spectra of V_2O_5 films annealed in air and nitrogen at 300 °C for 3 h; the inset presents a photograph of films after annealing in air (left) and nitrogen (right) at 300 °C for 3 h. (b) The Li$^+$ intercalation discharge capacities of V_2O_5 films annealed in air and N_2 at 300 °C for 3 h as a function of cycle number. The potential was ranging from 0.6 V to −1.4 V *vs.* Ag/Ag$^+$ at a current density of 600 mA g^{-1}.[94]

capacity of air annealed films dropped drastically from 152 mAh/g for the 1st cycle to 44 mAh/g for the 50th cycle. Interestingly, the discharge capacity of N_2 annealed films started low at 68 mAh/g for the 1st cycle, and rapidly increase to154 mAh/g at the 20th cycle then retained 148 mAh/g at the 50th cycle. The enhanced intercalation capacity with good cyclic stability could be explained not only by crystallinity, but also by the surface defects, such as V^{4+} or V^{3+} species and associated oxygen vacancies in the N_2 annealed films, which could (1) improve the electrical conductivity and electrolyte–electrode interfacial charge transfer ability;[95] (2) act as coating layers preventing the possible dissolution of V_2O_5 films in the electrolyte and ensuring integrity of film surface morphology after cycles;[7] (3) serve as nucleation centers in the phase transitions during Li^+ intercalation/deintercalation.[113] Similar phenomena were observed in nanostructured V_2O_5 films with surface defects.[109,114]

The anodization derived TiO_2 nanotube arrays were calcined at 400 °C for 3 h in respective dry gas flows of N_2 and CO.[112] The electrochemical impedance spectra of CO and N_2 annealed nanotube arrays are shown in Fig. 16 (a) and the electrode resistance and charge-transfer resistance were calculated to be 66 Ω and 38 Ω for N_2 annealed TiO_2 nanotube arrays, and 60 Ω and 26 Ω for CO annealed TiO_2 nanotube arrays, which indicated a higher charge-transfer rate of Li^+ in the electrode of CO annealed TiO_2 nanotubes. The XPS result (Fig. 16 (b)) of the

Ti2p spectrum of CO annealed TiO_2 nanotube arrays proved the existence of a small amount of Ti^{3+} (~456.8 eV) and Ti–C (~454.9 eV) in addition to the two characteristic Ti^{4+} peaks of $Ti2p_{1/2}$ at ~465 eV and $Ti2p_{3/2}$ at ~459 eV.[115,116] The improved charge-transfer conductivity of CO annealed TiO_2 nanotube arrays observed in the impedance study could be attributed to the presence of surface Ti–C species and Ti^{3+} and oxygen vacancy groups detected in XPS.[117,118]

The cyclic stability studies of N_2 and CO annealed TiO_2 nanotube arrays for Li^+ intercalation are shown in Fig. 16 (c) and it was found that the CO annealed TiO_2 nanotube arrays possessed a high Li^+ intercalation capacity of 223 mAh/g in the initial cycle and retained 179 mAh/g after 50 cycles, which was higher than N_2 annealed TiO_2 nanotube arrays with 164 mAh/g and 145 mAh/g for the 1st and 50th cycles. A comparison of rate intercalation capability between CO and N_2 annealed TiO_2 nanotube arrays (Fig. 16 (d)) showed that the intercalation capacity of N_2 annealed nanotube arrays reduced more rapidly than CO annealed ones, and the CO annealed nanotube arrays approximately doubled the intercalation capacities at higher rate, e.g. 101 mAh/g and 50 mAh/g at 10 A g^{-1} for CO and N_2 annealed TiO_2 nanotube arrays respectively. The much enhanced Li^+ intercalation properties in CO annealed TiO_2 nanotube arrays could be explained by the increased electrical conductivity and facilitated phase transition during Li^+ intercalation/
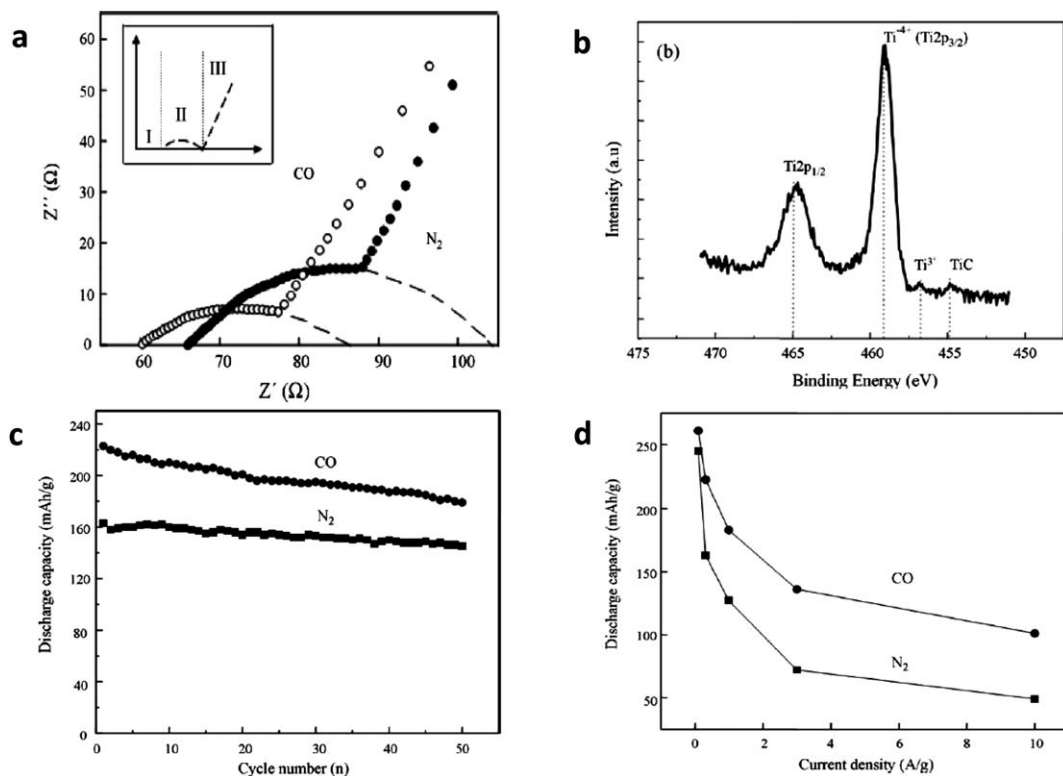
Fig. 16 (a) Electrochemical impedance spectra presented as Nyquist plots of titania nanotube arrays annealed in N_2 and CO at 400 °C for 3 h and measured in 1 M $LiClO_4$ in propylene carbonate with testing frequencies from 100 kHz to 0.05 Hz. The inset depicts the ideal impedance curve representing the Li^+ intercalation process into electrodes. (b) Ti2p XPS spectra of TiO_2 nanotube arrays annealed in CO gas at 500 °C for 3 h with Ti–C species and Ti^{3+} state detected. (c) The Li^+ intercalation capacity at 320 mA g^{-1} of TiO_2 nanotube arrays annealed in N_2 and CO at 400 °C for 3 h as a function of cycle number. (d) The initial discharge capacities of TiO_2 nanotube arrays annealed in N_2 and CO at 400 °C for 3 h as a function of applied discharge current density.[112]

deintercalation by the presence of surface defects, Ti–C species and Ti^{3+} with oxygen vacancies, which could facilitate charge transport accompanying rapid intercalation reactions at the interface. Moreover these defects could serve as nucleation sites to promote phase transitions during Li$^+$ intercalation and this results in a higher intercalation capacity under high current densities.

Doping is one of the most effective methods to introduce and distribute defects homogeneously into the bulk of materials. Mn^{2+} was directly doped into V$_2$O$_5$ films during sol preparation, and XPS results showed that there was ~18% of V^{4+} in the Mn-doped V$_2$O$_5$, and the presence of V^{4+} was most probably associated with oxygen vacancies by charge compensation. [93] Fig. 17 presents the Li$^+$ intercalation capacity as a function of current density for V$_2$O$_5$ films and Mn-doped V$_2$O$_5$ films. It clearly shows that the discharge capacity of Mn-doped V$_2$O$_5$ films is higher than that of undoped V$_2$O$_5$ films at identical current density, which demonstrates a better kinetics and much improved rate capability in Mn-doped V$_2$O$_5$ films compared to undoped V$_2$O$_5$ films. The cyclic performance after many cycles of Li$^+$ insertion/extraction in Mn-doped V$_2$O$_5$ films is also better than the undoped V$_2$O$_5$ films (Fig. 11 (b)). The excellent intercalation property in Mn-doped V$_2$O$_5$ films can be ascribed to the following three aspects: (1) the presence of oxygen vacancies could result in the formation of more open structure and easy access for Li$^+$ intercalation and

Fig. 17 Relationship between discharge capacity and current density for undoped V$_2$O$_5$ and Mn-doped V$_2$O$_5$, the potential was ranging from 0.5 V to −1.4 V *vs.* Ag/Ag$^+$. [93]

diffusion, which results in better cyclic stability and faster intercalation; (2) the oxygen vacancies may serve as possible nucleation centers for phase transition offering more intercalation sites; (3) the conductivity of Mn-doped V$_2$O$_5$ can also be enhanced owing to the presence of lower valence vanadium ions and associated oxygen vacancies, which could be beneficial for charge transfer during Li$^+$ intercalation/deintercalation.

The sol–gel route derived LiFePO$_4$/C nanocomposite films were introduced in previous sections for their excellent Li$^+$ intercalation performance due to their nanostructure and poor crystallinity. [49] In this section, we will discuss the electrochemical properties from the third aspect—carbon nanocoating as surface defects. A schematic drawing (Fig. 18 (a)) demonstrates the distribution and co-existence of carbon with LiFePO$_4$. The carbon residue from ascorbic acid forms an amorphous nano-network in LiFePO$_4$/C nanocomposite films, connecting the individual LiFePO$_4$ particles; carbon also wraps around the LiFePO$_4$ particles, and acts as both a nano-coating to improve the electrical conductivity and surface defect to enhance the Li$^+$ diffusion. The conventional electrode process adds 15–20 wt% of conductive additives (carbon black *etc.*) and binder (PVDF *etc.*) to the active materials with particle sizes of micrometre scale, which often gives an inadequate contact between particles thus impeding the effective Li$^+$ diffusion in certain areas. In addition, the additives and binders bring in noticeable mass which further results in a low specific energy and power density counted for the whole electrode. In contrast to the conventional configuration, the carbon network and nano-coating introduced by sol–gel chemistry in this work guarantees a better electrical conductivity, enhanced Li$^+$ diffusion and higher electrochemical performance as discussed below.

The charge–discharge performance at different charging rates of LiFePO$_4$/C nanocomposite film cathodes annealed at 600 °C is shown in Fig. 18 (b). The as-prepared LiFePO$_4$/C nanocomposite film cathodes demonstrate a high initial specific discharge capacity of 327 mAh/g at a current density of 100 mA g^{-1} (0.6 C). When the current density is 200 mA g^{-1} (1.2 C), the initial capacity is 312 mAh/g, and the initial capacities show 171 mAh/g and 139 mAh/g at higher rates of 300 mA g^{-1} (1.8 C) and 500 mA g^{-1} (3 C) respectively. The high discharge capacity at fast intercalation rates in LiFePO$_4$/C nanocomposite films could
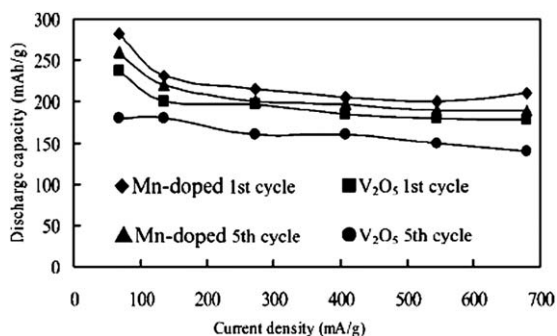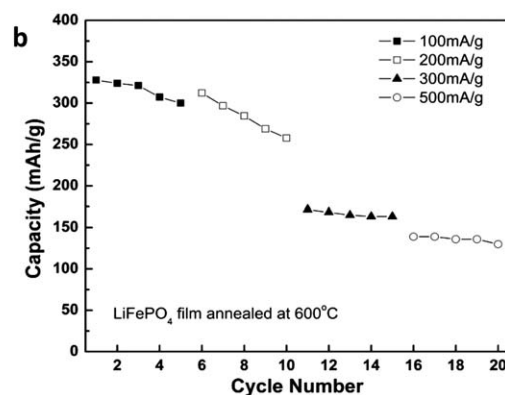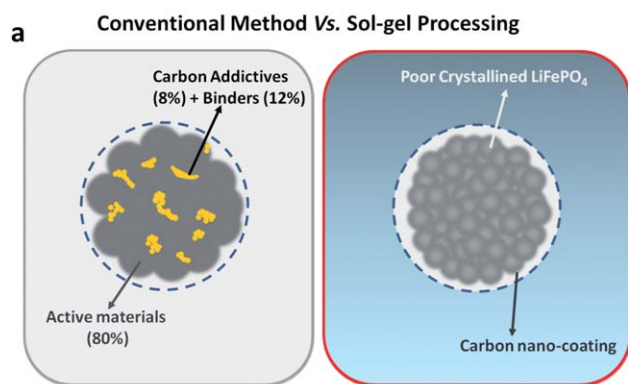
Fig. 18 (a) A schematic drawing comparing traditional electrode composed of active materials, conductive additives and binders (left), and sol–gel derived LiFePO$_4$/C nanocomposite cathode films, with LiFePO$_4$ nanocrystallites and carbon nanocoating (right). (b) Li$^+$ intercalation capacities of sol–gel derived LiFePO$_4$/C nanocomposite cathode films annealed at 600 °C as a function of cycles under different discharge rates. [49]

be explained not only by the nano-sized $LiFePO_4$ crystallites and poor crystallinity, but also the carbon nano-coating wrapping around $LiFePO_4$ particles. Serving as both surface defect and enhanced electronic conductive layer, the carbon nano-coating is beneficial for nucleation, phase transition and charge transfer, which are the three main processes during Li^+ intercalation/deintercalation.

5. Concluding remarks

This feature article summarized the most updated studies in our group, on constructing nanostructured electrode materials, controlling crystallinity of materials and manipulating surface defects to achieve much enhanced Li^+ intercalation properties. The nanostructured electrode materials can possess much enhanced Li^+ intercalation performance due to the large surface energy favoring the phase transition and reduced diffusion path providing improved transport properties. In addition, the extraordinarily large surface area offers better accessibility to the electrolyte resulting in more intercalation sites. Nanostructured electrodes also allow the easy volume change accompanied with the Li^+ insertion and extraction. Electrode materials with poor crystallinity and/or bulk or surface defects all exhibit better Li^+ intercalation properties, due to their higher energy state, more open structure, and more reaction sites. The electrode materials, nanostructured or with poor crystallinity or with defects, described in this paper all possess higher Gibbs free energy than that of a perfect bulk crystal counterpart; in other words, they are all far from thermodynamic equilibrium. The electrodes away from equilibrium may offer a new direction of research for the advancement of electroactive materials to achieve much improved Li^+ intercalation properties and, thus, lead to the development of more efficient Li-ion batteries.

Acknowledgements

References

1 N. Armaroli and V. Balzani, *Angew. Chem., Int. Ed.*, 2007, **46**, 52–66.
2 J. M. Tarascon, N. Recham, M. Armand, J. N. Chotard, P. Barpanda, W. Walker and L. Dupont, *Chem. Mater.*, 2010, **22**, 724–739.
3 J. M. Tarascon and M. Armand, *Nature*, 2001, **414**, 359–367.
4 D. Linden and T. B. Reddy, *Handbook Of Batteries* McGraw-Hill, New York, 2002.
5 B. E. Conway, *Electrochemical supercapacitors, Scientific fundamentals and technological applications*, Kluwer Academic/Plenum Publishers, New York, 1999.
6 G. Z. Cao, *Nanostructures and Nanomaterials, Synthesis, Properties and Applications*, Imperial College, London, 2004.
7 Y. Wang and G. Z. Cao, *Adv. Mater.*, 2008, **20**, 2251–2269.
8 M. Armand and J. M. Tarascon, *Nature*, 2008, **451**, 652–657.
9 P. G. Bruce, *Solid State Ionics*, 2008, **179**, 752–760.
10 D. W. Liu and G. Z. Cao, *Energy Environ. Sci.*, 2010, **3**, 1218–1237.
11 J. Liu, G. Z. Cao, Z. G. Yang, D. H. Wang, D. Dubois, X. D. Zhou, G. L. Graff, L. R. Pederson and J. G. Zhang, *ChemSusChem*, 2008, **1**, 676–697.
12 X. Z. Ren, Y. K. Jiang, P. X. Zhang, J. H. Liu and Q. L. Zhang, *J. Sol-Gel Sci. Technol.*, 2009, **51**, 133–138.
13 C. M. Ban, N. A. Chernova and M. S. Whittingham, *Electrochem. Commun.*, 2009, **11**, 522–525.
14 C. K. Chan, H. L. Peng, R. D. Twesten, K. Jarausch, X. F. Zhang and Y. Cui, *Nano Lett.*, 2007, **7**, 490–495.
15 S. W. Lee, N. Yabuuchi, B. M. Gallant, S. Chen, B. S. Kim, P. T. Hammond and Y. Shao-Horn, *Nat. Nanotechnol.*, 2010, **5**, 531–537.
16 A. K. Padhi, K. S. Nanjundaswamy and J. B. Goodenough, *J. Electrochem. Soc.*, 1997, **144**, 1188–1194.
17 A. K. Padhi, K. S. Nanjundaswamy, C. Masquelier, S. Okada and J. B. Goodenough, *J. Electrochem. Soc.*, 1997, **144**, 1609–1613.
18 Y. G. Wang, Y. R. Wang, E. J. Hosono, K. X. Wang and H. S. Zhou, *Angew. Chem., Int. Ed.*, 2008, **47**, 7461–7465.
19 J. K. Kim, G. Cheruvally and J. H. Ahn, *J. Solid State Electrochem.*, 2008, **12**, 799–805.
20 S. Y. Chung, J. T. Bloking and Y. M. Chiang, *Nat. Mater.*, 2002, **1**, 123–128.
21 Y. H. Huang and J. B. Goodenough, *Chem. Mater.*, 2008, **20**, 7237–7241.
22 F. Y. Cheng, J. Z. Zhao, W. Song, C. S. Li, H. Ma, J. Chen and P. W. Shen, *Inorg. Chem.*, 2006, **45**, 2038–2044.
23 H. R. Chen, X. P. Dong, J. L. Shi, J. J. Zhao, Z. L. Hua, J. H. Gao, M. L. Ruan and D. S. Yan, *J. Mater. Chem.*, 2007, **17**, 855–860.
24 J. W. Fergus, *J. Power Sources*, 2010, **195**, 939–954.
25 D. Jugovic and D. Uskokovic, *J. Power Sources*, 2009, **190**, 538–544.
26 M. Yoo, C. W. Frank, S. Mori and S. Yamaguchi, *Chem. Mater.*, 2004, **16**, 1945–1953.
27 H. K. Kim, T. Y. Seong and Y. S. Yoon, *Electrochem. Solid-State Lett.*, 2002, **5**, A252–A255.
28 N. Kuwata, J. Kawamura, K. Toribami, T. Hattori and N. Sata, *Electrochem. Commun.*, 2004, **6**, 417–421.
29 C. H. Chen, E. M. Kelder and J. Schoonman, *Thin Solid Films*, 1999, **342**, 35–41.
30 C. J. Brinker and G. W. Scherer, *Sol–Gel Science: The Physics and Chemistry of Sol–Gel Processing*, Academic Press, 1990.
31 G. Z. Cao, *J. Phys. Chem. B*, 2004, **108**, 19921–19931.
32 Y. Wang, K. Takahashi, K. Lee and G. Z. Cao, *Adv. Funct. Mater.*, 2006, **16**, 1133–1144.
33 Y. Wang and G. Z. Cao, *Electrochim. Acta*, 2006, **51**, 4865–4872.
34 K. Takahashi, S. J. Limmer, Y. Wang and G. Z. Cao, *J. Phys. Chem. B*, 2004, **108**, 9795–9800.
35 K. Takahashi, S. J. Limmer, Y. Wang and G. Z. Cao, *Jpn. J. Appl. Phys. Part 1-Regul. Pap. Brief Commun. Rev. Pap.*, 2005, **44**, 662–668.
36 K. Takahashi, Y. Wang and G. Z. Cao, *Appl. Phys. Lett.*, 2005, **86**.
37 Y. Wang, K. Takahashi, H. M. Shang and G. Z. Cao, *J. Phys. Chem. B*, 2005, **109**, 3085–3088.
38 K. Takahashi, Y. Wang and G. Z. Cao, *J. Phys. Chem. B*, 2005, **109**, 48–51.
39 Y. Wang, H. M. Shang, T. Chou and G. Z. Cao, *J. Phys. Chem. B*, 2005, **109**, 11361–11366.
40 A. S. Arico, P. Bruce, B. Scrosati, J. M. Tarascon and W. Van Schalkwijk, *Nat. Mater.*, 2005, **4**, 366–377.
41 J. Maier, *Nat. Mater.*, 2005, **4**, 805–815.
42 K. Takahashi, Y. Wang, K. Lee and G. Cao, *Appl. Phys. A: Mater. Sci. Process.*, 2006, **82**, 27–31.
43 K. Lee and G. Z. Cao, *J. Phys. Chem. B*, 2005, **109**, 11880–11885.
44 Y. Wang and G. Z. Cao, *Chem. Mater.*, 2006, **18**, 2787–2804.
45 D. W. Liu, Q. F. Zhang, P. Xiao, B. B. Garcia, Q. Guo, R. Champion and G. Z. Cao, *Chem. Mater.*, 2008, **20**, 1376–1380.
46 D. W. Liu, B. B. Garcia, Q. F. Zhang, Q. Guo, Y. H. Zhang, S. Sepehri and G. Z. Cao, *Adv. Funct. Mater.*, 2009, **19**, 1015–1023.
47 D. M. Yu, C. G. Chen, S. H. Xie, Y. Y. Liu, K. S. Park, X. Y. Zhou, Q. F. Zhang, J. Y. Li and G. Z. Cao, *Energy Environ. Sci.*, 2011, DOI: 10.1039/c0ee00313a, in press.
48 Y. Y. Liu, M. Clark, Q. F. Zhang, D. M. Yu, D. W. Liu, J. Liu and G. Z. Cao, *Advanced Energy Materials*, 2011, DOI: 10.1002/aenm.201000037, in press.
49 Y. Liu, D. Liu, Q. Zhang, D. Yu, J. Liu and G. Cao, *Electrochim. Acta*, 2011, **56**, 2559–2565.

50 M. S. Whittingham and P. Y. Zavalij, *Solid State Ionics*, 2000, **131**, 109–115.
51 M. H. Rossouw, D. C. Liles, M. M. Thackeray, W. I. F. David and S. Hull, *Mater. Res. Bull.*, 1992, **27**, 221–230.
52 C. S. Johnson, D. W. Dees, M. F. Mansuetto, M. M. Thackeray, D. R. Vissers, D. Argyriou, C. K. Loong and L. Christensen, *J. Power Sources*, 1998, **75**, 183–184.
53 H. E. Wang, D. Qian, Z. G. Lu, Y. K. Li, R. J. Cheng and Y. J. Li, *J. Phys. Chem. Solids*, 2007, **68**, 1422–1427.
54 F. Jiao and P. G. Bruce, *Adv. Mater.*, 2007, **19**, 657–660.
55 S. M. Zhu, H. A. Zhou, M. Hibino, I. Honma and M. Ichihara, *Adv. Funct. Mater.*, 2005, **15**, 381–386.
56 W. J. Zhou, J. Zhang, T. Xue, D. D. Zhao and H. L. Li, *J. Mater. Chem.*, 2008, **18**, 905–910.
57 D. H. Park, S. H. Lee, T. W. Kim, S. T. Lim, S. J. Hwang, Y. S. Yoon, Y. H. Lee and J. H. Choy, *Adv. Funct. Mater.*, 2007, **17**, 2949–2956.
58 H. M. Chen, J. H. He, C. B. Zhang and H. He, *J. Phys. Chem. C*, 2007, **111**, 18033–18038.
59 K. Le Van, H. Groult, A. Mantoux, L. Perrigaud, F. Lantelme, R. Lindstrom, R. Badour-Hadjean, S. Zanna and D. Lincot, *J. Power Sources*, 2006, **160**, 592–601.
60 C. Navone, J. P. Pereira-Ramos, R. Baddour-Hadjean and R. Salot, *J. Electrochem. Soc.*, 2006, **153**, A2287–A2293.
61 L. Wang, H. W. Xu, P. C. Chen, D. W. Zhang, C. X. Ding and C. H. Chen, *J. Power Sources*, 2009, **193**, 846–850.
62 Y. Yu, J. L. Shui and C. H. Chen, *Solid State Commun.*, 2005, **135**, 485–489.
63 X. H. Huang, J. P. Tu, X. H. Xia, X. L. Wang, J. Y. Xiang, L. Zhang and Y. Zhou, *J. Power Sources*, 2009, **188**, 588–591.
64 C. Delmas, H. Cognacauradou, J. M. Cocciantelli, M. Menetrier and J. P. Doumerc, *Solid State Ionics*, 1994, **69**, 257–264.
65 C. Delmas, S. Brethes and M. Menetrier, *J. Power Sources*, 1991, **34**, 113–118.
66 C. Leger, S. Bach, P. Soudan and J. P. Pereira-Ramos, *J. Electrochem. Soc.*, 2005, **152**, A236–A241.
67 T. Ohzuku, A. Ueda, M. Nagayama, Y. Iwakoshi and H. Komori, *Electrochim. Acta*, 1993, **38**, 1159–1167.
68 Z. H. Li, D. M. Zhang and F. X. Yang, *J. Mater. Sci.*, 2009, **44**, 2435–2443.
69 K. S. Kang, Y. S. Meng, J. Breger, C. P. Grey and G. Ceder, *Science*, 2006, **311**, 977–980.
70 A. R. Armstrong, D. W. Tee, F. La Mantia, P. Novak and P. G. Bruce, *J. Am. Chem. Soc.*, 2008, **130**, 3554–3559.
71 J. M. Tarascon and D. Guyomard, *Electrochim. Acta*, 1993, **38**, 1221–1231.
72 G. Pistoia and G. Wang, *Solid State Ionics*, 1993, **66**, 135–142.
73 D. Li and Y. Xia, *Adv. Mater.*, 2004, **16**, 1151–1170.
74 J. Y. Luo, J. J. Zhang and Y. Y. Xia, *Chem. Mater.*, 2006, **18**, 5618–5623.
75 M. Thommes, *Annual Review of Nano Research*, World Scientific, Singapore, 2009.
76 E. Potiron, A. L. La Salle, A. Verbaere, Y. Piffard and D. Guyomard, *Electrochim. Acta*, 1999, **45**, 197–214.
77 O. W. Howarth and J. R. Hunt, *J. Chem. Soc., Dalton Trans.*, 1979, 1388–1391.
78 C. J. Fontenot, J. W. Wiench, M. Pruski and G. L. Schrader, *J. Phys. Chem. B*, 2001, **105**, 10496–10504.
79 C. J. Fontenot, J. W. Wiench, M. Pruski and G. L. Schrader, *J. Phys. Chem. B*, 2000, **104**, 11622–11631.
80 E. Potiron, A. Le Gal La Salle, S. Sarciaux, Y. Piffard and D. Guyomard, *J. Power Sources*, 1999, **81–82**, 666–669.
81 P. Liu, S. H. Lee, C. E. Tracy, Y. F. Yan and J. A. Turner, *Adv. Mater.*, 2002, **14**, 27–30.
82 V. Srinivasan and J. Newman, *Electrochem. Solid-State Lett.*, 2006, **9**, A110–A114.
83 N. Meethong, H. Y. S. Huang, W. C. Carter and Y. M. Chiang, *Electrochem. Solid-State Lett.*, 2007, **10**, A134–A138.
84 C. Delacourt, P. Poizot, S. Levasseur and C. Masquelier, *Electrochem. Solid-State Lett.*, 2006, **9**, A352–A355.
85 X. D. Yan, G. L. Yang, J. Liu, Y. C. Ge, H. M. Xie, X. M. Pan and R. S. Wang, *Electrochim. Acta*, 2009, **54**, 5770–5774.
86 D. J. Reidy, J. D. Holmes and M. A. Morris, *J. Eur. Ceram. Soc.*, 2006, **26**, 1527–1534.
87 J.-y. Luo, Y.-g. Wang, H.-m. Xiong and Y.-y. Xia, *Chem. Mater.*, 2007, **19**, 4791–4795.
88 H. Yang, X.-L. Wu, M.-H. Cao and Y.-G. Guo, *J. Phys. Chem. C*, 2009, **113**, 3345–3351.
89 H. Zhang, G. R. Li, L. P. An, T. Y. Yan, X. P. Gao and H. Y. Zhu, *J. Phys. Chem. C*, 2007, **111**, 6143–6148.
90 J. Wang, J. Polleux, J. Lim and B. Dunn, *J. Phys. Chem. C*, 2007, **111**, 14925–14931.
91 C.-M. Park and H.-J. Sohn, *Adv. Mater.*, 2010, **22**, 47–52.
92 W. C. West, N. V. Myung, J. F. Whitacre and B. V. Ratnakumar, *J. Power Sources*, 2004, **126**, 203–206.
93 D. M. Yu, S. T. Zhang, D. W. Liu, X. Y. Zhou, S. H. Xie, Q. F. Zhang, Y. Y. Liu and G. Z. Cao, *J. Mater. Chem.*, 2010, **20**, 10841–10846.
94 D. W. Liu, Y. Y. Liu, B. B. Garcia, Q. F. Zhang, A. Q. Pan, Y. H. Jeong and G. Z. Cao, *J. Mater. Chem.*, 2009, **19**, 8789–8795.
95 D. W. Liu, P. Xiao, Y. H. Zhang, B. B. Garcia, Q. F. Zhang, Q. Guo, R. Champion and G. Z. Cao, *J. Phys. Chem. C*, 2008, **112**, 11175–11180.
96 A. Q. Pan, D. W. Liu, X. Y. Zhou, B. B. Garcia, S. Q. Liang, J. Liu and G. Z. Cao, *J. Power Sources*, 2010, **195**, 3893–3899.
97 Y. J. Wei, C. W. Ryu and K. B. Kim, *J. Power Sources*, 2007, **165**, 386–392.
98 S. Y. Zhan, C. Z. Wang, K. Nikolowski, H. Ehrenberg, G. Chen and Y. J. Wei, *Solid State Ionics*, 2009, **180**, 1198–1203.
99 B. Kang and G. Ceder, *Nature*, 2009, **458**, 190–193.
100 P. Xiao, B. B. Garcia, Q. Guo, D. W. Liu and G. Z. Cao, *Electrochem. Commun.*, 2007, **9**, 2441–2447.
101 D. H. Kim, H. W. Ryu, J. H. Moon and J. Kim, *J. Power Sources*, 2006, **163**, 196–200.
102 A. Feaver, S. Sepehri, P. Shamberger, A. Stowe, T. Autrey and G. Z. Cao, *J. Phys. Chem. B*, 2007, **111**, 7469–7472.
103 B. B. Garcia, A. M. Feaver, Q. F. Zhang, R. D. Champion, G. Z. Cao, T. T. Fister, K. P. Nagle and G. T. Seidler, *J. Appl. Phys.*, 2008, **104**.
104 S. Sepehri, B. B. Garcia and G. Z. Cao, *Eur. J. Inorg. Chem.*, 2009, 599–603.
105 S. Sepehri, B. B. Garcia, Q. F. Zhang and G. Z. Cao, *Carbon*, 2009, **47**, 1436–1443.
106 Y. S. Hu, X. Liu, J. O. Muller, R. Schlogl, J. Maier and D. S. Su, *Angew. Chem., Int. Ed.*, 2009, **48**, 210–214.
107 A. M. Cao, J. S. Hu, H. P. Liang and L. J. Wan, *Angew. Chem., Int. Ed.*, 2005, **44**, 4391–4395.
108 D. H. Wang, D. W. Choi, J. Li, Z. G. Yang, Z. M. Nie, R. Kou, D. H. Hu, C. M. Wang, L. V. Saraf, J. G. Zhang, I. A. Aksay and J. Liu, *ACS Nano*, 2009, **3**, 907–914.
109 K. E. Swider-Lyons, C. T. Love and D. R. Rolison, *Solid State Ionics*, 2002, **152–153**, 99–104.
110 D. R. Rolison and B. Dunn, *J. Mater. Chem.*, 2001, **11**, 963–980.
111 N. Meethong, Y. H. Kao, S. A. Speakman and Y. M. Chiang, *Adv. Funct. Mater.*, 2009, **19**, 1060–1070.
112 D. W. Liu, Y. H. Zhang, P. Xiao, B. B. Garcia, Q. F. Zhang, X. Y. Zhou, Y. H. Jeong and G. Z. Cao, *Electrochim. Acta*, 2009, **54**, 6816–6820.
113 H. S. Jung, H. Shin, J. R. Kim, J. Y. Kim and K. S. Hong, *Langmuir*, 2004, **20**, 11732–11737.
114 D. Sun, C. W. Kwon, G. Baure, E. Richman, J. MacLean, B. Dunn and S. H. Tolbert, *Adv. Funct. Mater.*, 2004, **14**, 1197–1204.
115 J. M. Macak, H. Tsuchiya and P. Schmuki, *Angew. Chem., Int. Ed.*, 2005, **44**, 2100–2102.
116 J. Zhao, E. G. Garza, K. Lam and C. M. Jones, *Appl. Surf. Sci.*, 2000, **158**, 246–251.
117 S. Petigny, H. Mostefa-Sba, B. Domenichini, E. Lesniewska, A. Steinbrunn and S. Bourgeois, *Surf. Sci.*, 1998, **410**, 250–257.
118 H. Nörenberg, F. Dinelli and G. A. D. Briggs, *Surf. Sci.*, 2000, **446**, L83–L88.

This journal is © The Royal Society of Chemistry 2011

J. Mater. Chem., 2011, **21**, 9969–9983 | 9983